small methods
www.small-methods.com

In situ Sub-Cellular Identification of Functional Amyloids in Bacteria and Archaea by Infrared Nanospectroscopy

Daniel E. Otzen, Morten S. Dueholm, Zahra Najarzadeh, Tuomas P. J. Knowles, and Francesco Simone Ruggeri**

Formation of amyloid structures is originally linked to human disease. However, amyloid materials are found extensively in the animal and bacterial world where they stabilize intra- and extra-cellular environments like biofilms or cell envelopes. To date, functional amyloids have largely been studied using optical microscopy techniques in vivo, or after removal from their biological context for higher-resolution studies in vitro. Furthermore, conventional microscopies only indirectly identify amyloids based on morphology or unspecific amyloid dyes. Here, the high chemical and spatial (≈20 nm) resolution of Infrared Nanospectroscopy (AFM-IR) to investigate functional amyloid from *Escherichia coli* (curli), *Pseudomonas* (Fap), and the Archaea *Methanosaeta* (MspA) in situ is exploited. It is demonstrated that AFM-IR identifies amyloid protein within single intact cells through their cross β-sheet secondary structure, which has a unique spectroscopic signature in the amide I band of protein. Using this approach, nanoscale-resolved chemical images and spectra of purified curli and *Methanosaeta* cell wall sheaths are provided. The results highlight significant differences in secondary structure between *E. coli* cells with and without curli. Taken together, these results suggest that AFM-IR is a new and powerful label-free tool for in situ investigations of the biophysical state of functional amyloid and biomolecules in general.

1. Introduction

Many proteins are capable of associating to long filamentous assemblies called amyloids, in which intermolecular β-sheets from individual monomers are aligned orthogonal to the fibril axis (cross-β) with intermolecular interactions formed through a combination of hydrogen bonds and side chain interactions.[1] The consequences of these self-organizing processes can be deleterious or beneficial, depending on the context. In neurodegenerative diseases such as Parkinson's and Alzheimer's, amyloid accumulates as intra- or extra-cellular deposits of insoluble material, which are cytotoxic or at best inert biological waste material. However, there are also numerous cases where the amyloid state constitutes a useful and versatile physical state that contributes to function as diverse as intra- or extracellular architecture, protein/peptide reservoirs, information transmission and signaling.[2] These amyloid proteins have been evolutionarily optimized to efficiently and rapidly form self-assemblies without accumulating cytotoxic intermediates, unlike their disease-related counterparts.[3] In these cases, information about their precise cellular location and their impact on cellular properties such as mechanical stiffness has high biological relevance. The best-characterized bacterial functional amyloid is the curli system found in *E. coli*.[4] The major protein component CsgA is secreted to the bacterial surface via a dedicated export system involving the

Prof. D. E. Otzen, Dr. Z. Najarzadeh
Interdisciplinary Nanoscience Center (iNANO)
Aarhus University
Gustav Wieds Vej 14, Aarhus C, Aarhus 8000, Denmark
E-mail: dao@inano.au.dk
Dr. M. S. Dueholm
Department of Chemistry and Bioscience
Aalborg University
Fredrik Bajers Vej 7H, Aalborg 9220, Denmark
The ORCID identification number(s) for the author(s) of this article can be found under https://doi.org/10.1002/smtd.202001002.

DOI: 10.1002/smtd.202001002

Prof. T. P. J. Knowles, Dr. F. S. Ruggeri
Department of Chemistry
University of Cambridge
Cambridge CB2 1EW, UK
E-mail: simone.ruggeri@wur.nl
Prof. T. P. J. Knowles
Cavendish Laboratory
University of Cambridge
Cambridge CB30HE, UK
Dr. F. S. Ruggeri
Laboratory of Organic Chemistry
Wageningen University
Wageningen WE 6703, the Netherlands
Dr. F. S. Ruggeri
Laboratory of Physical Chemistry
Wageningen University
Wageningen WE 6703, the Netherlands

bacterial channel CsgG, a periplasmatic aggregation inhibitor CsgC, a putative channel "gatekeeper" CsgE and a bridging protein CsgF, which anchors the nucleator protein CsgB onto the bacterial outer membrane and the CsgG channel.[5] Thus once CsgA exits the CsgG channel on the bacterial cell surface, it can either attach directly to an available CsgB molecule to start a growing amyloid fibril or diffuse away to attach to the growing end of the fibril (or other nearby fibrils) extending away from the cell. Analogous systems have been found in *Pseudomonas* where the Functional amyloid in pseudomonas (Fap) system also involves a major amyloid component (FapC), an outer membrane channel (FapF), a putative nucleator (FapB) and other accessory components (FapA, FapD, FapE).[6] Once formed, these extracellular amyloid fibrils can protect the bacteria from drying out and increase the mechanical strength and hydrophobicity of the biofilm in which the bacterial cells are often embedded.[7]

Amyloid found in many different bacterial species[8] and has have also been discovered in Archaea. For example, individual cells of the methanogen *Methanosaeta*, which is a strict anaerobe, are encased in an extracellular cell wall sheath composed mainly of the major sheath protein (MspA), which adopts an amyloid fold.[9] MspA shows no homology to other functional amyloids, indicating that the amyloid fold is a motif that can be attained in vivo in many different ways. In all these cases, the amyloid nature of the protein deposits has been demonstrated through low-resolution approaches such as immunofluorescence using amyloid-specific antibodies,[8] electron microscopy (which is not structurally specific) or via purification and subsequent structural analysis of the putative amyloid component. Given the highly insoluble and often adhesive nature of structural amyloids such as curli and Fap fibrils, purification is not trivial and often constitutes a major bottleneck in the identification of novel amyloid components.[6a] Furthermore, purification removes the protein from its native environment and distorts information about the biological context, which is otherwise critical for a full appreciation of functional amyloids. Therefore, techniques that provide in situ spectroscopic information about protein structure at sub-micrometer resolution in an authentic cellular environment are very useful in the study of functional amyloid.

Nanoscale resolved microscopies, such as Electron Microscopy (EM) and Atomic Force Microscopy (AFM) have emerged as powerful and versatile techniques to study the morphology of biological specimens at the nanometer scale.[10] However, these nanoscale imaging methods are unable alone to directly correlate the morphological, mechanical and chemical properties of biomolecules within complex and heterogeneous cellular systems. Conversely, bulk and vibrational spectroscopies such as infrared (IR) and Raman are powerful tools for chemically characterizing materials, including biological samples and cells.[11] However, for studies of single cells, the diffraction-limited practical spatial resolution of commercial Fourier transform infrared (FT-IR (3–10 μm) or Raman (0.5 μm)) micro-spectrometers are not sufficient to characterize the inner distribution and structure of protein and biomolecules.

To overcome the prior limitations of vibrational spectroscopy and imaging techniques, several nanoscale spectroscopies based on scanning probe microscopy have been developed in the last decades, in particular scattering scanning near field optical microscopy (s-SNOM), tip-enhanced Raman spectroscopy (TERS) and infrared nanospectroscopy (AFM-IR).[12] TERS and s-SNOM techniques rely on the measurement of scattered light to acquire chemical information at the nanoscale, which can lead to unwanted chemical shifts and suppression of absorption peaks. In the case of s-SNOM, the acquired chemical spectra are susceptible to shifts in the position of absorption peaks causing deformation and artefacts, which are undesirable to unravel the properties of biological samples and determine protein structure.[13] While, in the case of TERS, spectra acquired from biological systems commonly lack the amide band I, which is of fundamental importance to study protein structure and interactions.[14] These factors have hampered the high-throughput and widespread application of TERS and s-SNOM to characterize protein structure, preventing further development of in situ measurements.[15]

On the other hand, Infrared Nanospectroscopy (AFM-IR) exploits the combination of the high spatial resolution of AFM (≈1–10 nm) with the chemical analysis power of IR spectroscopy and measures purely IR absorption of the sample by thermomechanical detection, which is proportional to the sample's absorption coefficient and independent of the properties of the sample and the AFM tip. The method exploits readily available commercial gold-coated AFM probes without the need for large enhancement factors, and the spectra produced are in excellent agreement with conventional bulk IR spectra.[16]

Over the last few years, AFM-IR has been widely applied in biology. It is now capable of simultaneously acquiring morphological, nanomechanical and nanoscale-resolved chemical IR absorption spectra and maps from single cells, chromosomes, protein aggregates, and liquid-liquid phase separated condensates.[16a,h,17] Furthermore, as a major advance in the field, we have demonstrated that off-resonance and short pulse AFM-IR (ORS-nanoIR) can acquire infrared maps and spectra to determine protein secondary structure down to the single protein molecule level.[15,18] The ultimate spatial resolution of maps and spectra acquisition in contact mode is in the order of 10–20 nm.[15] Its scanning properties also allow it to analyze complex mixtures with co-existing species such as amyloid, amorphous aggregates and pre-fibrillar aggregates, which differ in secondary structure.[16b,h,k,19]

To the best of our knowledge, AFM-IR has not been applied to investigate the structure of functional amyloid in situ. Here, we apply the high sensitivity and spatial resolution of AFM-IR to investigate the secondary and quaternary structure of functional amyloids in vitro and at the sub-cellular scale on *E. coli, Pseudomonas,* and *Methanosaeta* cells. We demonstrate that AFM-IR can record IR spectra on the nanometer scale of sufficient quality to obtain second derivative spectra that unambiguously demonstrate the amyloid nature of individual curli fibrils. Furthermore, the results reveal significant differences at the nanoscale in secondary structure between *E. coli* cells with and without curli, as well between the body and extracellular vesicles of pseudomonas cells. Finally, we confirm the amyloid nature of the cell wall sheaths of *Methanosaeta,* which show that the organism is essentially wrapped in an amyloid cocoon as originally hypothesized but not directly shown.[9]

2. Results

2.1. Nanoscale Chemical Mapping and Spectroscopy (AFM-IR) of Extracted *E. coli* Curli

A scheme illustrating the principle of function of the AFM-IR setup is shown in **Figure 1**a. A tunable laser is focused on the tip of the cantilever. If the wavenumber of the exciting laser radiation pulse matches one of the molecular vibrational energy transition levels of the protein, the IR light is absorbed. This absorption causes a thermal heating and expansion of the protein, which is detected by the AFM cantilever.[16a,17b,20] The IR absorbance at each wavenumber is proportional to the thermomechanical response of the cantilever, which can be measured as the peak-to-peak amplitude of the raw deflection of the cantilever oscillation (Figure 1a) and to the peak amplitude of its Fourier transform (IR amplitude). In the top illumination configuration, the peak-to-peak amplitude and IR amplitude are directly proportional to the IR absorption for samples with thickness of several micrometers.[21] This guarantees a linear response of the AFM-IR thermomechanical response in the case of thin films and bacteria investigated in this work, which have typical cross-sectional heights below 1 µm (Figure 1b). Furthermore, the AFM tip and the sample in contact behave as a system of coupled springs. The frequency contact resonance is the frequency of oscillation of the sample and cantilever in contact. Since the stiffness of the cantilever is fixed, a lower contact resonance corresponds to a softer sample, and a higher contact resonance to a stiffer sample.[16f] Overall, by scanning the sample while it is illuminated by IR light at constant wavenumber, AFM-IR allows to simultaneously map the morphology (Figure 1c), the IR absorption (Figure 1d) and the stiffness of the samples (Figure 1e). Once the mapping of the biophysical properties is completed, the AFM probe is positioned on specific locations on the sample and nanoscale resolved spectra are acquired (Figure 1f). In order to improve AFM-IR sensitivity, a resonance-enhanced and more recently an off-resonance modes have been further introduced.[15,17c] In these approaches, the frequency of the pulse of the IR laser is matched with the mechanical contact resonance frequency between the sample and the tip by selecting a laser pulse frequency leading to the maximum of the IR amplitude signal. In order to avoid cross-talk between

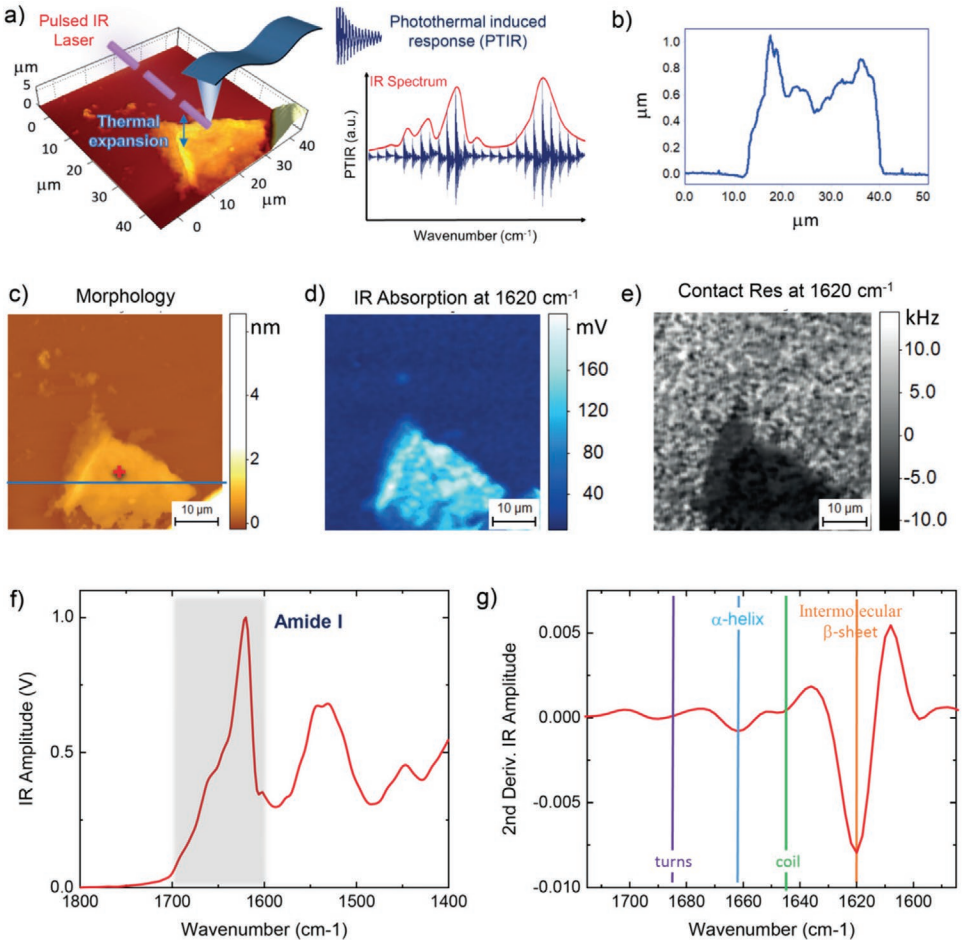

Figure 1. AFM-IR chemical and structural characterization of extracted curli fibrils from *E. coli*. a) Scheme of the experimental setup of AFM-IR used to study extracted functional amyloids and single cells.[27] b) Cross-sectional height of the film. The AFM-IR technique allows the simultaneous acquisition of the sample c) 3D morphology, d) IR Absorption, and e) Contact resonance frequency maps (stiffness) at a fixed wavenumber in the amide Band I of protein. f) Once the mapping is completed, the probe can be pointed at specific locations on the sample to acquire nanoscale localized (f) average IR spectra (AVG + SEM, $n = 6$) in the amide I region (1700–1600 cm^{-1}) and calculate g) their second derivative spectra to evaluate the secondary structure.

the chemical and mechanical information, we tracked during spectra and maps acquisition the contact resonance frequency between the tip and the sample by a phase-locked loop (PLL).[15] The high signal-to-noise ratio of the spectra allows to further calculate their second derivatives for band deconvolution.

The AFM-IR properties of isolated curli fibrils were initially determined and used as a reference for subsequent analyses. To ensure that the native structure of the curli fibrils was maintained, we applied a purification strategy that utilized enzymes and detergents to solubilize and remove contaminating cell macromolecules while the amyloids were kept in their native, insoluble form.[6a,22] The extracted curli protein self-assemblies adhered to the surface of the ZnSe substrate (Figure 1c–e). The biofilms attached material showed fairly uniform chemical and mechanical properties (Figure 1c–e). After chemical mapping, we collected nanoscale IR spectra and we observed that the amide band I of protein had a pronounced peak at ≈1620 cm^{-1} (Figure 1f); which indicated the presence of intermolecular hydrogen bonded amyloidogenic β-sheet, as suggested by previous studies.[16b,23] Then, we calculated the second derivatives of the absorption spectra to deconvolve the amide I band and quantify the secondary and quaternary structural contributions to the protein self-assembly structure (Figure 1g).[15,24] The structure of the purified curli was dominated by the presence of intermolecular parallel β-sheets (60%), residual β-turns (10%), random coil and/or α-helix conformations (30%).[15,16b]

Having characterized the chemical signature of purified curli, the next step was to use the AFM-IR approach to investigate the heterogeneous chemical properties of single *E. coli* cells at the nanoscale. We considered two different strains *E. coli* SM2278 (curli positive) and SM2257 (curli negative). The curli positive strain is a derivative of *E. coli* MC4100 that contains a mutation in the curli regulatory OmpR gene, which lead to the expression of curli fibrils under laboratory growth conditions.[25] The curli negative strain was derived from the curli positive strain by knocking out the *csgA* gene, which encodes the major curli subunit.[26] These properties makes the curli negative strain an ideal control for studying signal contribution from non-amyloid proteins and thus establish the best possible basis to evaluate the impact of curli on cellular structure.

2.2. *E. coli* Overproducing Curli Protein

The approach allowed us to map the morphology, IR absorption and stiffness related maps of single bacterial cells producing curli (**Figure 2**a–c). The stiffness map and the infrared map at the frequency of absorption of intermolecular parallel β-sheet (1620 cm^{-1}) revealed a heterogeneous response. In particular, the top part of the bacterium (orange circle) showed significantly higher contact resonance frequency (Figure 2d), thus indicating an increased content of intermolecular hydrogen-bonded β-sheet conformation and stiffness, when compared to the bottom part of the bacterium (red circle).

To demonstrate independently that the increase in stiffness is related to the increase of intermolecular β-sheet conformation, we acquired nanoscale resolved IR spectra on regions showing higher and lower contact resonance frequency (Figure 2e). The amide band I of the stiffer region (orange) showed reduced α-helix content and thus enhanced absorption in the spectroscopic signature of intermolecular β-sheet, respect to native proteins conformation (α-helix, random coil and β-turn), when compared to the softer region (red) (Figure 2f). These results demonstrate that we can successfully monitor the distribution of amyloid proteins at the sub-cellular scale. We then mapped the morphology and IR absorption of several different cells (**Figure 3**a,b). After this we acquired nanoscale localized IR spectra (Figure 3c, $n > 300$) and calculated their average spectra and associated second derivative in the amide band I (Figure 3d, $n > 300$). The results confirmed that the curli-producing cells contain a high proportion of intermolecular β-sheet conformation of amyloid protein (Figure 3d).

2.3. *E. coli* without Curli Production

We used an identical approach as in the previous paragraph to unravel the chemical signature of the *E. coli* curli negative control.[26] We first mapped the morphology and IR absorption of several ($n = 9$) bacteria (**Figure 4**a,b). Then, we acquired and averaged IR nanoscale localized IR spectra on 10 different locations (Figure 4c, $n > 150$), after which we calculated and averaged their second derivatives in the amide band I (Figure 4d). The deconvolution of the amide band I showed that for bacteria not producing curli, the predominant band of absorption is the one related to native α-helical and random coil conformation (1658–1640 cm^{-1}). In addition, we still observed content of intermolecular β-sheet, which we attribute to other non-amyloid proteins with extended beta-sheets in the bacteria, e.g., β-barrel membrane proteins.

2.4. Comparison of *E. coli* Cells with and without Curli

The acquisition of several maps and spectra on different cells allowed reducing the intra- and intercellular variability, providing a robust basis for comparison of the chemical and structural signatures of bacteria with and without curli. We first noticed that the morphology of the bacteria with and without curli showed fundamental differences. *E. coli* producing curli had a smooth topography and rigid shape, while the cells without curli had irregular topography, were smaller, and they were easily damaged by the AFM probe (Figure S1, Supporting Information). This suggests that the presence of the curli has an important function for cellular rigidity and stability. Similar phenotypes were previously observed for *Pseudomonas* with and without Fap expression.[7]

We then compared the average spectroscopic signatures of protein amide I for both *E. coli* strains based on multiple positions on different bacteria (**Figure 5**b, average (AVG) + standard error of mean (SEM)). In the IR spectra there is also a weaker peak at 1730 cm^{-1} which is assigned to the IR absorption of the C=O stretching of lipids. The relative amplitudes and area of the Amide I and the C=O stretching of lipids refer to their relative abundance; the *E. coli* producing curli showed a significantly smaller area of the C=O stretching of lipids, thus a lower relative content of lipids and slightly increased content of proteins. Subsequently, we compared

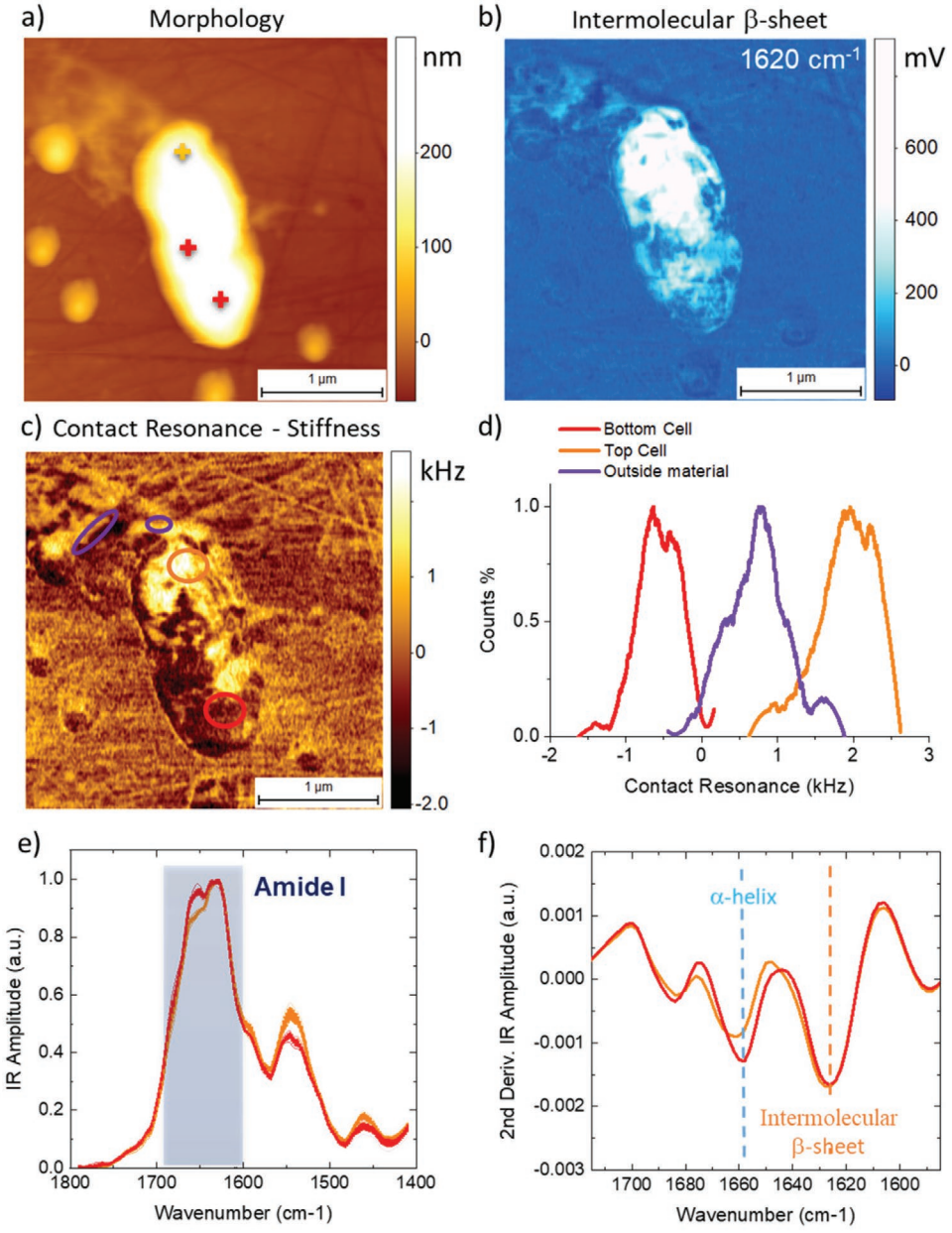

Figure 2. Morphological, chemical, and mechanical imaging of single *E. coli* cells overproducing curli by AFM-IR. a) 3D morphology map. b) IR absorption image at 1620 cm^{-1} (amide band I). c) Map of contact resonance frequency, related to stiffness, at 1620 cm^{-1}. d) Histogram distributions of contact resonance frequency in the top (orange), bottom (red), and outside the cell (violet). See corresponding circled areas in panel (c). e) IR spectra acquired on regions with higher (orange) and lower (red) stiffness (AVG + SEM; bottom $n = 100$, top $n = 0$) in the spectroscopic fingerprint of protein and f) their second derivatives to evaluate the secondary structure of protein in the bacteria.

the secondary structure of the protein content in *E. coli* with and without curli production. The second derivative of the average spectra showed that indeed the strain producing curli has an increased content of intermolecular β-sheet and a smaller amount of α-helical structure than *E. coli* lacking curli (Figure 5c, AVG + SEM). To further investigate the difference between the signature of the two *E. coli* strains and suppress spectroscopic contributions from other biological components, we subtracted the two average IR spectra from each other (Figure 5d). This difference spectrum clearly shows that curli production leads to a net increase of intermolecular β-sheet and decrease of native α-helix conformation. Finally, the integration of the structural contributions in the second derivatives enables us to quantify an increase of +10% for intermolecular β-sheet (Figure 5e). In contrast, bulk infrared spectroscopy was unable to distinguish between *E. coli* with and without curli (Figure S1, Supporting Information). Presumably, the averaging effects of examining large numbers of cells and extracellular material eclipse the differences between the two strains. This highlights the importance of being able to visualize individual cells and sections hereof to gauge significant differences in structure.

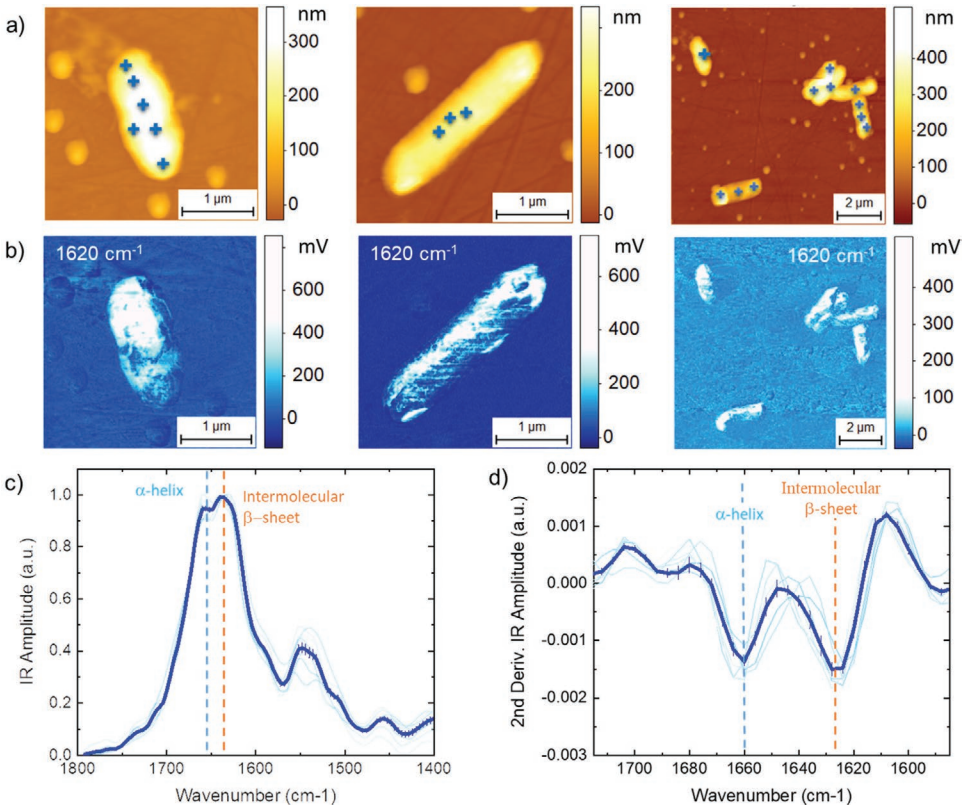

Figure 3. Average chemical properties of *E. coli* overproducing curli. a) 3D morphology and b) IR absorption maps at 1620 cm^{-1} (amide band I). c) Average IR spectra acquired on 8 different cells (AVG + SEM; $n > 250$ over 20 different positions on 8 different bacteria) in the spectroscopic fingerprint of protein and d) their second derivatives to evaluate the secondary structure of proteins in the bacteria.

Overall, the comparison of nanoscale versus bulk information emphasizes the importance of recording nanoscale localized AFM-IR spectra on individual bacteria to detect amyloid structures. The results on *E. coli* demonstrate at the single cell scale that functional curli, with the unique mechanical properties of amyloid stabilized by intermolecular hydrogen bonded β-sheets, has a fundamental role in providing structural integrity and resistance to mechanical stress to the cells.

2.5. AFM-IR of *Pseudomonas* Producing Fap and Outer Membrane Vesicles

To provide an additional in situ example of the exceptional capabilities of AFM-IR, we investigated the Fap model organism *Pseudomonas* sp. UK4 with plasmid-induced overexpression of the Fap system (Figure S3, Supporting Information).[6a] The bacterial cells displayed a high proportion of intermolecular β-sheet conformation indicative of amyloid protein, similar to our previous observations for the curli producing *E. coli* strain. Besides the bacterial cells, we also observed outer membrane vesicles (OMVs) produced by the bacterium. The nanoscale chemical resolution of AFM-IR enabled to unravel the different chemical composition of the cellular body and the OMVs. The chemical signature of these OMVs was markedly different from that of the bacterial cells, which is rich in protein signal, and had instead major chemical signatures relative to membrane lipids (1720–1730 cm^{-1}) and nucleic acids (1590 cm^{-1}). Detailed second derivative analysis of the amide I band of OMV finally revealed absence of signal related to intermolecular β-sheet conformation, thus demonstrating that Fap amyloids produced by the bacterium were not released with the OMVs.

2.6. AFM-IR Confirms the Amyloid Nature of *Methanosaeta* Cell Wall Sheaths

To demonstrate the general applicability of AFM-IR for functional amyloid characterization, we also examined with nanoscale chemical resolution the spectral and structural properties of single *Methanosaeta* cell filaments and extracted cell wall sheaths (**Figure 6**).[9]

We recorded the morphology of intact cells (Figure 6a) and then acquired nanoscale chemical spectra (Figure 6b). As observed in the second derivative spectra, the IR spectra present a clear signature of intermolecular β-sheet conformation (Figure 6c). To prove that the cells use functional amyloids as external coating, we isolated their cell wall sheaths (Figure 6d) and investigated their chemical and structural composition. The cell wall sheaths yielded a typical protein spectrum (Figure 6e), and second derivative analysis confirms that the sheaths have a high content of intermolecular hydrogen-bonded β-sheet (Figure 6f). Thus, we can confirm that these organisms make use of amyloids for their external coating. Remarkably, the

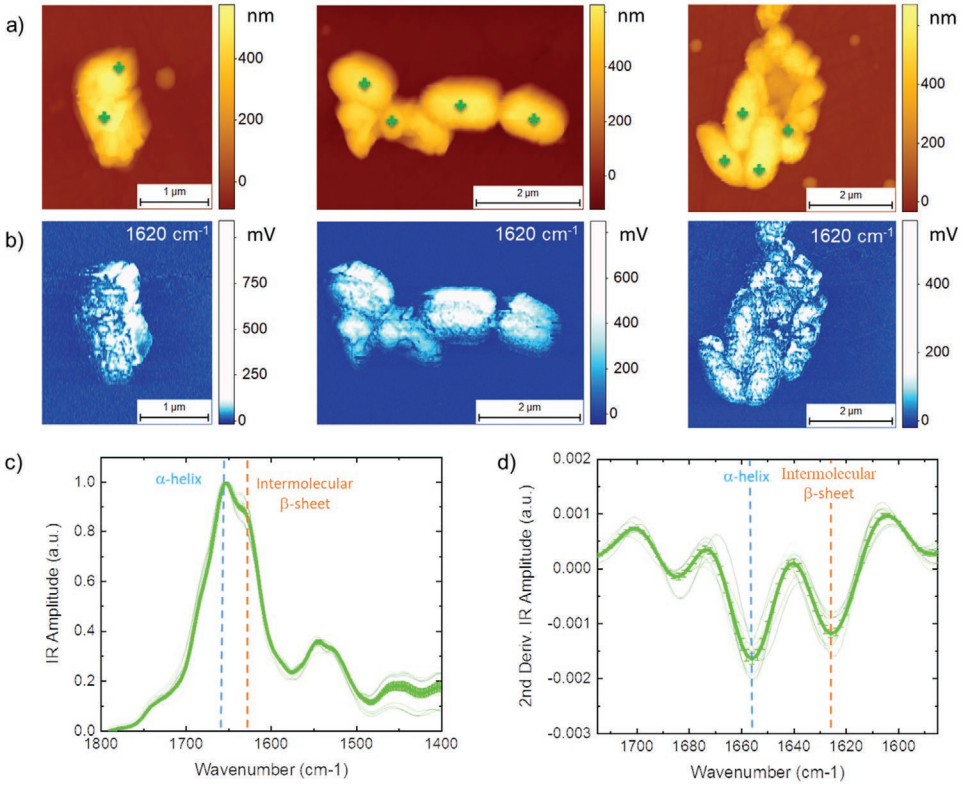

Figure 4. Average properties of *E. coli* without curli production. a) 3D morphology and b) IR absorption maps at 1620 cm^{-1} (amide band I). c) Average IR spectra acquired on 8 different cells (AVG + SEM; $n > 150$ over 10 different positions on 9 different bacteria) in the spectroscopic fingerprint of protein and d) their second derivatives to evaluate the secondary structure of protein in the bacteria.

cell surface of the intact cells has an even more evident intermolecular peak at 1620 cm^{-1} than the extracted sheaths, indicating that amyloid is a very prominent part of the whole cell structure.

3. Conclusion

A major objective of Biology is to understand how biomolecules, and in particular protein, fulfil their biological functions in vivo, both in physiological and pathological states. Biophysical studies on proteins, their functional and pathological self-assemblies and their properties are not only of fundamental importance for science but also has medical and technological applications with great impact on society.

For the first time, here, we demonstrate the existence of amyloid structure in intact *E. coli* and *Pseudomonas* bacterial cells through in situ nanoscale analysis of their sub-cellular spectroscopic signature and of their secondary structure content. We demonstrate that AFM-IR is sufficiently accurate to distinguish between bacteria and cellular components with and without functional amyloid. Furthermore, we confirm the highly amyloidogenic nature of the cell wall sheaths of the archaea *Methanosaeta,* which effectively acts as an "amyloid cocoon." Thus, our work provides insight into both the structure and cellular context of these functional amyloids.

Until now, the level of information provided by our work at the nanoscale was not directly accessible by any other available biophysical approach, and the amyloid-like nature of these aggregates has been only indirectly suggested and with low-resolution spectroscopic techniques.

In the future, we envision the application of the approach presented in this work to study not only functional self-assemblies in micro- and macro-organisms but also protein inclusions in cellular and animal models of neurodegeneration. For this scope, it would also be particularly attractive to couple AFM-IR to other biophysical techniques enabling accurate determination of protein identity and composition, such as nanoscale mass spectrometry, to provide an identification of proteins of interest. Overall, AFM-IR will be an excellent tool for future investigations of functional amyloid in natural and pathology contexts.

4. Experimental Section

Sample Preparation: The *E. coli* curli deletion mutant SM2257 (*csgDAB::Kan*),[26] the curli positive strain SM2258 (OmpR 234 Tc^R),[25] and *Pseudomonas* sp. UK4 transformed with the pMMB190Tc-UK4fap plasmid[6a] were grown for 3 days at 26 °C in colonization factor antigen (CFA) medium (10 g L^{-1} hydrolyzed casein, 50 mg L^{-1} $MgSO_4$, 5 mg L^{-1} $MnCl_2$, 1.5 g L^{-1} yeast extract, pH 7.4). The grown cultures were stored at

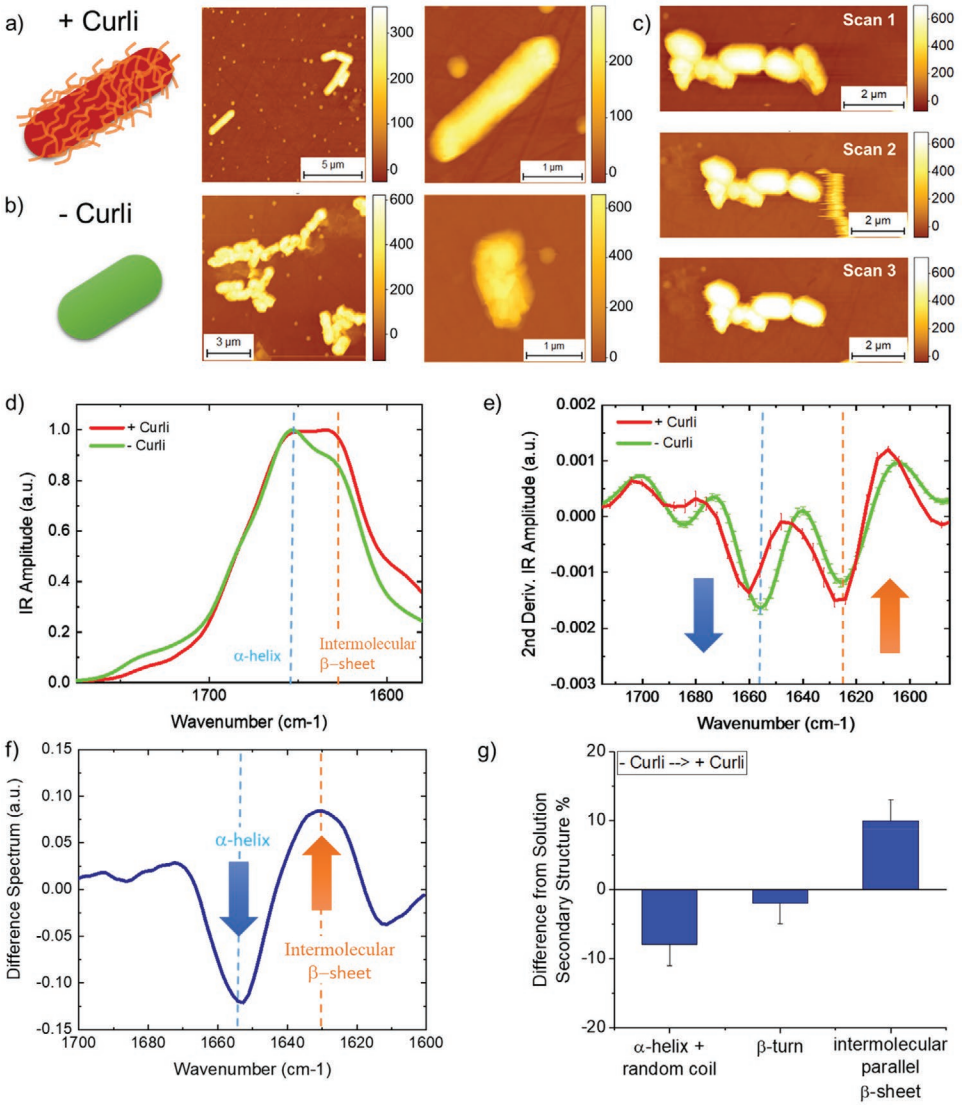

Figure 5. Comparison of the spectroscopic signature of *E. coli* with and without curli. a) *E. coli* producing curli. b) *E. coli* without curli production, and c) damage inflicted over three consecutive AFM scans. Average + SEM d) IR spectra and e) second derivatives in the amide band I. The two arrows indicate the effect of curli production on the spectra. f) Difference of the average IR spectra in the amide I region (red curve minus green curve from figure (e). Arrows highlight areas with significant change. g) Difference in secondary structure as quantified by integrating the second derivatives as described in Experimental Section.

–80 °C in 30% v/v glycerol. The glycerol stocks were thawed and washed three times with distilled water before AFM-IR analyses. Curli fibrils were obtained from a previous study.[6a]

Methanosaeta thermophila: PT (DSM 6194) were obtained from the German Collection of Microorganisms and Cell Cultures (DSMZ) and cultured in DSMZ medium 387 according to the instructions provided by DSMZ. The cells were harvested by centrifugation and washed twice in 50% v/v ethanol and stored at –18 °C. Cell wall sheaths were obtained from a previous study.[9]

AFM-IR Measurements, Maps Treatment and Analysis: A nanoIR1 and nanoIR2 platforms (Anasys, USA), which combines high resolution and low noise AFM with tunable quantum cascade (QCL) and optical parametric oscillator (OPO) lasers with both bottom and top illumination configurations were used. The samples morphology was scanned by the nanoIR microscopy system, with a rate line within 0.1–0.4 Hz and in contact mode. A silicon gold coated PR-EX-nIR2 (Anasys, USA) cantilever with a nominal radius of 30 nm and an elastic constant of about 0.2 N m^{-1} was used. Resonance enhanced spectra and maps were acquired by using phase loop (PLL) tracking of contact resonance, the phase was set to zero to the desired off-resonant frequency on the left of the IR amplitude maximum, and tracked with an integral gain I = 0.1 and proportional gain P = 5.[27] All images were acquired with a resolution between 500 × 200 and 1000 × 1000 pixels per line. The AFM images were treated and analyzed using SPIP software. The height images were first order flattened, while IR and stiffness related maps where only flattened by a zero-order algorithm (offset).

Nanoscale localized spectra were collected by placing the AFM tip on the top of cell with a laser wavelength sampling between 1–4 cm^{-1} and 256 co-averages, within the range 1400–1800 cm^{-1}. The spectra were smoothed first by adjacent averaging (3–5 points), Savitzky-Golay filter (second order, 9–15 points) and normalized

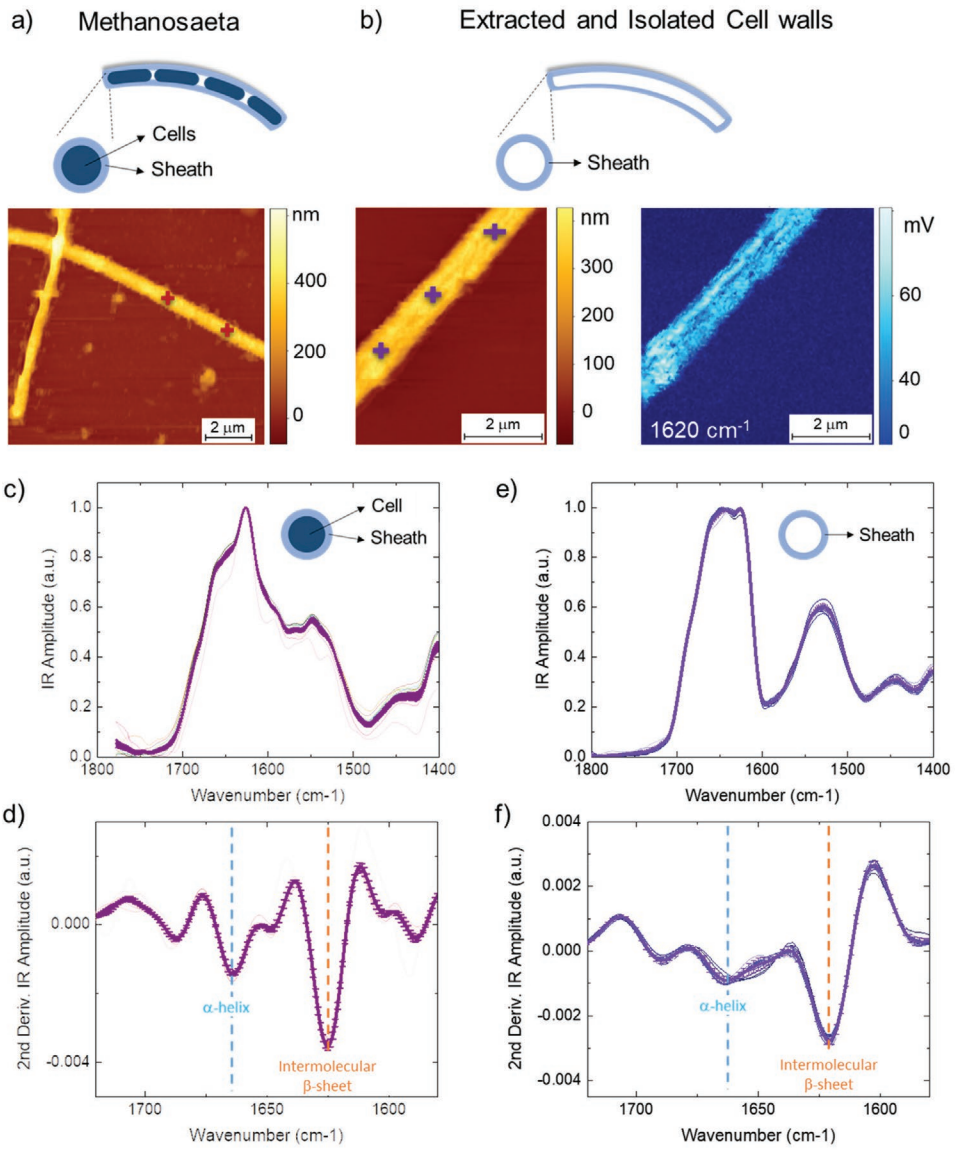

Figure 6. AFM-IR the archaea *Methanosaeta*. Comparison of the morphology of a) *Methanosaeta* cell filaments and b) extracted cell wall sheaths with their chemical response at 1620 cm^{-1}. Average + SEM of the IR spectra and second derivatives in the amide band I of c,d) *Methanosaeta* cells and e,f) extracted cell walls ($n = 12$ and $n = 15$).

to the maximum. Spectra second derivatives were calculated, smoothed by Savitzky-Golay filter (second order, 15 points). Relative secondary and quaternary organization was evaluated by integrating the area of the different secondary structural contribution in the amide band I, as previously described.[16b,28] The error in the determination of the relative secondary structure content, calculated over an average of at least 5 independent spectra, is <5%. Spectra were analyzed using the microscope's built-in Analysis Studio (Anasys) and OriginPRO. All measurements were performed at room temperature and with laser power between 1% and 20% of the maximal one[15] and under a controlled nitrogen atmosphere with residual real humidity below 5%.

Supporting Information

Supporting Information is available from the Wiley Online Library or from the author.

Acknowledgements

F.S.R. is supported by Darwin College, Cambridge. D.E.O. is supported by the Independent Research Foundation Denmark | Natural Sciences (grant 8021-00208B) and the Independent Research Foundation Denmark | Technology and Production (grant 6111-00241B). M.S.D. is supported by the Villum Foundation (grant 13351).

Conflict of Interest

The authors declare no conflict of interest.

Data Availability Statement

The data that support the findings of this study are available from the corresponding authors upon reasonable request.

Keywords

AFM-IR, archaeal cell wall sheaths, curli, functional amyloids

Received: October 26, 2020
Revised: March 16, 2021
Published online:

[1] P. C. Ke, R. Zhou, L. C. Serpell, R. Riek, T. J. Knowles, H. A. Lashuel, E. Gazit, I. W. Hamley, T. P. Davis, D. E. Otzen, M. R. Chapman, C. M. Dobson, D. Eisenberg, R. Mezzenga, *Chem. Soc. Rev.* **2020**, *49*, 5473.

[2] a) D. E. Otzen, R. Riek, *Cold Spring Harb Perspect Biol* **2019**, *11*, 033860; b) M. Dueholm, P. H. Nielsen, M. R. Chapman, D. E. Otzen, in *Amyloid Fibrils and Prefibrillar Aggregates* (Ed: D. E. Otzen), Wiley-VCH Verlag GmbH, Weinheim **2012**, pp. 411–438.

[3] P. Alam, L. Bousset, R. Melki, D. E. Otzen, *J. Neurochem.* **2019**, *150*, 522.

[4] a) M. R. Chapman, L. S. Robinson, J. S. Pinkner, R. Roth, J. Heuser, M. Hammar, S. Normark, S. J. Hultgren, *Science* **2002**, *295*, 851; b) M. Hammar, A. Arnqvist, Z. Bian, A. Olsen, S. Normark, *Mol. Microbiol.* **1995**, *18*, 661.

[5] L. F. B. Christensen, N. Schafer, A. Wolf-Perez, D. J. Madsen, D. E. Otzen, *Adv. Exp. Med. Biol.* **2019**, *1174*, 113.

[6] a) M. S. Dueholm, S. V. Petersen, M. Sønderkær, P. Larsen, G. Christiansen, K. L. Hein, J. J. Enghild, J. L. Nielsen, K. L. Nielsen, P. H. Halkjær, D. E. Otzen, *Mol. Microbiol.* **2010**, *77*, 1009; b) S. L. Rouse, W. J. Hawthorne, J.-L. Berry, D. S. Chorev, S. A. Ionescu, S. Lambert, F. Stylianou, W. Ewert, U. Mackie, R. M. L. Morgan, D. Otzen, F.-A. Herbst, P. H. Nielsen, M. Dueholm, H. Bayley, C. V. Robinson, S. Hare, S. Matthews, *Nat. Commun.* **2017**, *8*, 263.

[7] G. Zeng, B. S. Vad, M. S. Dueholm, G. Christiansen, M. Nilsson, T. Tolker-Nielsen, P. H. Nielsen, R. L. Meyer, D. E. Otzen, *Front. Microbiol.* **2015**, *6*, 1099.

[8] P. Larsen, M. Dueholm, G. Christiansen, J. L. Nielsen, D. E. Otzen, P. H. Nielsen, *Environ. Microbiol.* **2007**, *9*, 3077.

[9] M. S. Dueholm, P. Larsen, K. Finster, M. R. Stenvang, G. Christiansen, B. S. Vad, A. Bøggild, D. E. Otzen, P. H. Nielsen, *J. Biol. Chem.* **2015**, *290*, 20590.

[10] a) B. Cappella, G. Dietler, *Surf. Sci. Rep.* **1999**, *34*, 1; b) M. Girasole, S. Dinarelli, G. Boumis, *Micron* **2012**, *43*, 1273; c) M. Girasole, G. Pompeo, A. Cricenti, G. Longo, G. Boumis, A. Bellelli, S. Amiconi, *Nanomedicine* **2010**, *6*, 760; d) E. Kozlova, A. Chernysh, V. Moroz, V. Sergunova, O. Gudkova, E. Manchenko, *Sci. Rep.* **2017**, *7*, 7846.

[11] a) A. Derenne, T. Claessens, C. Conus, E. Goormaghtigh, in *Encyclopedia of Biophysics* (Ed: G. C. K. Roberts), Springer, Berlin, Heidelberg, **2013**, pp. 1074–1081; b) B. H. Stuart, *Infrared Spectroscopy: Fundamentals and Applications*, Wiley, Chichester, UK **2005**.

[12] a) C. Blum, T. Schmid, L. Opilik, S. Weidmann, S. R. Fagerer, R. Zenobi, *J. Raman Spectrosc.* **2012**, *43*, 1895; b) R. M. Stöckle, Y. D. Suh, V. Deckert, R. Zenobi, *Chem. Phys. Lett.* **2000**, *318*, 131; c) F. Zenhausern, M. P. O'Boyle, H. K. Wickramasinghe, *Appl. Phys. Lett.* **1994**, *65*, 1623; d) E. A. Muller, B. Pollard, M. B. Raschke, *J. Phys. Chem. Lett.* **2015**, *6*, 1275.

[13] S. Mastel, A. A. Govyadinov, T. V. A. G. d. Oliveira, I. Amenabar, R. Hillenbrand, *Appl. Phys. Lett.* **2015**, *106*, 023113.

[14] a) D. Kurouski, T. Postiglione, T. Deckert-Gaudig, V. Deckert, I. K. Lednev, *Analyst* **2013**, *138*, 1665; b) C. Blum, T. Schmid, L. Opilik, N. Metanis, S. Weidmann, R. Zenobi, *J. Phys. Chem. C* **2012**, *116*, 23061.

[15] F. S. Ruggeri, B. Mannini, R. Schmid, M. Vendruscolo, T. P. J. Knowles, *Nat. Commun.* **2020**, *11*, 2945.

[16] a) A. Dazzi, C. B. Prater, *Chem. Rev.* **2017**, *117*, 5146; b) F. S. Ruggeri, G. Longo, S. Faggiano, E. Lipiec, A. Pastore, G. Dietler, *Nat. Commun.* **2015**, *6*, 7831; c) T. Muller, F. S. Ruggeri, A. J. Kulik, U. Shimanovich, T. O. Mason, T. P. Knowles, G. Dietler, *Lab Chip* **2014**, *14*, 1315; d) S. Qamar, G. Wang, S. J. Randle, F. S. Ruggeri, J. A. Varela, J. Q. Lin, E. C. Phillips, A. Miyashita, D. Williams, F. Strohl, W. Meadows, R. Ferry, V. J. Dardov, G. G. Tartaglia, L. A. Farrer, G. S. Kaminski Schierle, C. F. Kaminski, C. E. Holt, P. E. Fraser, G. Schmitt-Ulms, D. Klenerman, T. Knowles, M. Vendruscolo, P. St George-Hyslop, *Cell* **2018**, *173*, 720; e) F. S. Ruggeri, C. Marcott, S. Dinarelli, G. Longo, M. Girasole, G. Dietler, T. P. J. Knowles, *Int. J. Mol. Sci.* **2018**, *19*, 2582; f) L. R. Volpatti, U. Shimanovich, F. S. Ruggeri, S. Bolisetty, T. Muller, T. O. Mason, T. C. T. Michaels, R. Mezzenga, G. Dietler, T. P. J. Knowles, *J. Mater. Chem. B* **2016**, *4*, 7989; g) F. Simone Ruggeri, J. Habchi, A. Cerreta, G. Dietler, *Curr. Pharm. Des.* **2016**, *22*, 3950; h) F. S. Ruggeri, S. Vieweg, U. Cendrowska, G. Longo, A. Chiki, H. A. Lashuel, G. Dietler, *Sci. Rep.* **2016**, *6*, 31155; i) F. S. Ruggeri, C. Byrne, L. Khemtemourian, G. Ducouret, G. Dietler, Y. Jacquot, *J. Pept. Sci.* **2015**, *21*, 95; j) A. Centrone, in *Annual Review of Analytical Chemistry, Vol. 8* (Eds: R. G. Cooks, J. E. Pemberton), Annual Reviews, Palo Alto, **2015**, pp. 101–126; k) D. Galante, F. S. Ruggeri, G. Dietler, F. Pellistri, E. Gatta, A. Corsaro, T. Florio, A. Perico, C. D'Arrigo, *Int. J. Biochem. Cell Biol.* **2016**, *79*, 261.

[17] a) G. Ramer, F. S. Ruggeri, A. Levin, T. P. J. Knowles, A. Centrone, *ACS Nano* **2018**, *12*, 6612; b) F. S. Ruggeri, J. Habchi, A. Cerreta, G. Dietler, *Curr. Pharm. Des.* **2016**, *22*, 3950; c) F. Lu, M. Z. Jin, M. A. Belkin, *Nat. Photonics* **2014**, *8*, 307; d) F. S. Ruggeri, J. Habchi, S. Chia, R. I. Horne, M. Vendruscolo, T. P. J. Knowles, *Nat. Commun.* **2021**, *12*, 688; e) J. Adamcik, F. S. Ruggeri, J. T. Berryman, A. Zhang, T. P. J. Knowles, R. Mezzenga, *Adv. Sci.* **2021**, *8*, 2002182.

[18] T. Marchesi D'Alvise, S. Harvey, L. Hueske, J. Szelwicka, L. Veith, T. P. J. Knowles, D. Kubiczek, C. Flaig, F. Port, K. E. Gottschalk, F. Rosenau, B. Graczykowski, G. Fytas, F. S. Ruggeri, K. Wunderlich, T. Weil, *Adv. Funct. Mater.* **2020**, *30*, 2000378.

[19] J. Waeytens, V. Van Hemelryck, A. Deniset-Besseau, J. M. Ruysschaert, A. Dazzi, V. Raussens, *Molecules* **2020**, *25*, 2899.

[20] F. Lu, M. Jin, M. A. Belkin, *Nat. Photonics* **2014**, *8*, 307.

[21] B. Lahiri, G. Holland, A. Centrone, *Small* **2013**, 439.

[22] M. S. Dueholm, S. B. Nielsen, K. L. Hein, P. Nissen, M. Chapman, G. Christiansen, P. H. Nielsen, D. E. Otzen, *Biochemistry* **2011**, *50*, 8281.

[23] G. Zandomeneghi, M. R. Krebs, M. G. McCammon, M. Fändrich, *Protein Sci.* **2004**, *13*, 3314.

[24] H. Yang, S. Yang, J. Kong, A. Dong, S. Yu, *Nat. Protoc.* **2015**, *10*, 382.

[25] O. Vidal, R. Longin, C. Prigent-Combaret, C. Dorel, M. Hooreman, P. Lejeune, *J. Bacteriol.* **1998**, *180*, 2442.

[26] C. Prigent-Combaret, G. Prensier, T. T. Le Thi, O. Vidal, P. Lejeune, C. Dorel, *Environ. Microbiol.* **2000**, *2*, 450.

[27] F. S. Ruggeri, T. Sneideris, S. Chia, M. Vendruscolo, T. P. J. Knowles, *J. Visualized Exp.* **2019**, *12*, https://doi.org/10.3791/60108.

[28] a) S. Qamar, G. Wang, S. J. Randle, F. S. Ruggeri, J. A. Varela, J. Q. Lin, E. C. Phillips, A. Miyashita, D. Williams, F. Strohl, W. Meadows, R. Ferry, V. J. Dardov, G. G. Tartaglia, L. A. Farrer, G. S. Kaminski Schierle, C. F. Kaminski, C. E. Holt, P. E. Fraser, G. Schmitt-Ulms, D. Klenerman, T. Knowles, M. Vendruscolo, P. St George-Hyslop, *Cell* **2018**, *173*, 720; b) U. Shimanovich, F. S. Ruggeri, E. De Genst, J. Adamcik, T. P. Barros, D. Porter, T. Muller, R. Mezzenga, C. M. Dobson, F. Vollrath, C. Holland, T. P. J. Knowles, *Nat. Commun.* **2017**, *8*, 15902.